



Published in final edited form as:

Ultrasound Med Biol. 2011 March ; 37(3): 345–357. doi:10.1016/j.ultrasmedbio.2010.11.020.

Three-dimensional High-frequency Backscatter and Envelope Quantification of Cancerous Human Lymph Nodes

Jonathan Mamou^a, Alain Coron^{b,c}, Michael L. Oelze^d, Emi Saegusa Beecroft^e, Masaki Hata^e, Paul Lee^a, Junji Machi^e, Eugene Yanagihara^e, Pascal Laugier^{b,c}, and Ernest J. Feleppa^a

^aF. L. Lizzi Center for Biomedical Engineering, Riverside Research Institute, New York, NY

^bUPMC Univ Paris 06, UMR 7623, LIP, Paris, F-75005 France

^cCNRS, UMR 7623 Laboratoire d'Imagerie Paramétrique, Paris, F-75006 France

^dBioacoustics Research Laboratory, Department of Electrical and Computer Engineering, University of Illinois, Urbana, IL

^eUniversity of Hawaii and Kuakini Medical Center, Honolulu, HI

Abstract

Quantitative imaging methods using high-frequency ultrasound (HFU) offer a means of characterizing biological tissue at the microscopic level. Previously, high-frequency, three-dimensional (3D) quantitative-ultrasound (QUS) methods were developed to characterize 46 freshly-dissected lymph nodes of colorectal-cancer patients. 3D ultrasound radio-frequency data were acquired using a 25.6-MHz center-frequency transducer and each node was inked prior to tissue fixation to recover orientation after sectioning for 3D histological evaluation. Backscattered echo signals were processed using 3D cylindrical regions-of-interest (ROIs) to yield four QUS estimates associated with tissue microstructure (i.e., effective scatterer size, acoustic concentration, intercept, and slope). These QUS estimates, obtained by parameterizing the backscatter spectrum, showed great potential for cancer detection. In the present study, these QUS methods were applied to 112 lymph nodes from 77 colorectal and gastric cancer patients. Novel QUS methods parameterizing the envelope statistics of the ROIs using Nakagami and homodyned-K distributions also were developed; they yielded four additional QUS estimates. The ability of these eight QUS estimates to classify lymph nodes and detect cancer was evaluated using ROC curves. An area under the ROC curve of 0.996 with specificity and sensitivity of 95% were obtained by combining effective scatterer size and one envelope parameter based on the homodyned-K distribution. Therefore, these advanced 3D QUS methods potentially can be valuable for detecting small metastatic foci in dissected lymph nodes.

Keywords

High-frequency ultrasound; quantitative ultrasound; lymph nodes; micrometastases; cancer

© 2011 World Federation for Ultrasound in Medicine and Biology. Published by Elsevier Inc. All rights reserved.

Contact author: Jonathan Mamou F. L. Lizzi Center for Biomedical Engineering Riverside Research Institute 156 William St., 9th floor New York, NY 10038 212-502-1755 FAX: 212-502-1729 jmamou@rri-usa.org.

Publisher's Disclaimer: This is a PDF file of an unedited manuscript that has been accepted for publication. As a service to our customers we are providing this early version of the manuscript. The manuscript will undergo copyediting, typesetting, and review of the resulting proof before it is published in its final citable form. Please note that during the production process errors may be discovered which could affect the content, and all legal disclaimers that apply to the journal pertain.

INTRODUCTION

High-frequency (i.e., >15 MHz) ultrasound (HFU) permits investigating biological tissue at microscopic levels with spatial resolutions on the order of 100 μm . Recent, successful HFU studies have permitted imaging shallow or low-attenuation tissues for biomedical applications. For instance, HFU already has been successfully used for small-animal (Turnbull, 2000; Turnbull and Foster, 2002; Aristizábal et al, 1998; Mamou et al, 2009a), ocular (Silverman et al, 2008, 1995), intravascular (de Korte et al, 2000; Saijo et al, 2004), and dermatological imaging (Vogt and Ermert, 2007; Huang et al, 2007).

Our group has demonstrated the ability of quantitative ultrasound (QUS) to characterize lymph-node tissues from cancer patients (Mamou et al, 2010). Reliable determination of the presence or absence of metastatic cancer in lymph nodes is essential for staging disease and planning its treatment. Most human lymph nodes have sizes ranging from 2 to 10 mm in diameter and are sufficiently small to be imaged in their entirety in three dimensions (3D) using HFU. The long-term objective of our lymph-node studies is to develop QUS imaging methods that are capable of detecting small nodal metastases using echo-signal data from freshly-excised nodes for staging disease in patients who have known primary cancers in neighboring organs (e.g., breast, colon, stomach, etc.). In routine pathology procedures, this method would direct the pathologist to suspicious regions that might be overlooked in conventional histology. In sentinel-node procedures, the method would serve as a basis for identifying sentinel nodes, detecting metastatic cancer, and initiating formal (i.e., complete) node dissections when sentinel nodes are positive for cancer. To achieve this long-term objective, QUS studies that were previously undertaken successfully (Mamou et al, 2010) have been improved, refined to include envelope statistics, and applied to a larger number of lymph nodes.

This manuscript focuses on two different categories of QUS methods. The first category quantifies the backscattered spectrum deduced from the radio-frequency (RF) echo signals and the second category quantifies the statistics of the envelope-detected echo signals. The spectral methods were first established by Lizzi et al (1983), and since this foundation work, many others (Insana et al, 1990; Feleppa et al, 1986; Oelze et al, 2002; Oelze and Zachary, 2006; Mamou et al, 2008, 2010) have pushed this field forward and developed methods for tissue characterization and cell characterization (Kolios et al, 2002; Baddour et al, 2005). In these studies, the frequency-dependent backscattered information was used to assess tissue microstructural properties quantitatively and relate them to histological properties (Insana et al, 1990; Feleppa et al, 1986; Oelze et al, 2002). In particular, our group recently has shown promising results using backscatter-derived QUS estimates for the detection of metastases in freshly-dissected lymph nodes from colorectal-cancer patients (Mamou et al, 2010).

Many QUS studies have also been performed by modeling the envelope statistics for tissue characterization. These methods fit a specific distribution model to the observed distribution of the envelope-detected signals statistics. QUS estimates are obtained from the fit parameters, and similar to the QUS methods from backscatter quantification, the hypothesis is that these envelope-statistics-based QUS estimates provide a means of distinguishing between different tissue types. Many different distribution models (e.g., Rayleigh, K, Nakagami, etc.) have been used for ultrasound tissue characterization (Wagner et al, 1987; Shankar et al, 2000, 2001; Shankar, 2000). In a recent HFU study, the generalized gamma distribution showed promise at detecting structural changes during cell death in acute myeloid leukemia cells (Tunis et al, 2005).

In our studies, we decided to use the homodyned-K (HK) distribution. This distribution is more involved computationally, but it can model more-complex ultrasound scattering

situations (Dutt and Greenleaf, 1994; Hao et al, 2002). All the previously-mentioned distribution models, their relationships to one another, and their physical interpretation recently have been theoretically studied and described (Destrempes and Cloutier, 2010); this study concluded that the HK distribution is the only model for which the distribution parameters retain a physical meaning in the case where the diffuse scattering vanishes. Additionally, the HK distribution can model low scatterer densities correctly and also can quantify the coherent component in backscattered signals that originates from organized (sub-resolution) scatterers (Destrempes and Cloutier, 2010). Because of its analytical complexity, the HK distribution model has been criticized (Shankar, 2000; Eltoft, 2005; Tsui and Chang, 2007), and its use has been somewhat limited while other, more analytically tractable models such as the Nakagami distribution (Shankar, 2000; Tsui and Chang, 2007), Weibull distribution (Raju and Srinivasan, 2002), Rician inverse Gaussian distribution (Eltoft, 2005), and the generalized gamma distribution (Raju and Srinivasan, 2002) have been used. The HK distribution is defined by three independent parameters: 1) the μ parameter, which quantifies the number of scatterers per resolution cell, 2) the s parameter, which quantifies the coherent signal, and 3) the σ parameter, which quantifies the incoherent signal. A fourth parameter, the k parameter, is the ratio of the coherent to in-coherent signal components. The richness of the parameterization improves interpretation of results when compared to estimates from other distributions, e.g., the Nakagami distribution, which is a function of only two parameters. Nevertheless, in a recent study, the HK distribution was used in conjunction with computationally-extensive algorithms to characterize cardiac tissues (Hao et al, 2002). More recently, a new parameter-estimation algorithm for the HK distribution was developed that is efficient and robust (Hruska et al, 2009; Hruska and Oelze, 2009). This improved parameter-estimation algorithm provides more accurate information to elucidate better the relationships between the envelope statistics and the underlying structures responsible for the signals. In the present study, the ability of the HK distribution to quantify lymph-node properties was assessed and fit parameters using the Nakagami distribution were also obtained for comparison. The Nakagami distribution had shown success in characterizing breast masses and was used here as a reasonable, high-quality reference (Shankar et al, 2001; Tsui et al, 2010).

The current standard histopathology procedure for lymph-node evaluation has many limitations, and the possibility of detecting easily-overlooked but clinically significant small metastases, particularly metastases that have a size between 0.2 and 2 mm) in excised lymph nodes using QUS approaches in quasi real-time, could be valuable in mitigating these limitations. Currently, most lymph nodes dissected from a cancer patient either are sent to pathology for a postoperative thorough histological preparation and evaluation, or they first undergo a rapid intraoperative “touch-prep” procedure (e.g., for sentinel nodes of breast-cancer patients). Neither approach is able to detect all small metastases in lymph nodes, particularly micrometastases. Furthermore, the touch-prep approach produces a large number of false-negative determinations because the pathologist only examines cells exfoliated from two adjacent surfaces of the lymph node, and the cells derived from these surfaces may not reveal the presence of a small cancerous region within a metastatic node. Additionally, a thorough histology preparation takes several days to produce results because several thin sections are evaluated by a pathologist, but it suffers fewer false-negative determinations.

The remainder of the present paper is organized into the following three sections: the Methods section briefly reviews our methods from surgery and lymph-node preparation to QUS image formation and presents the new methods for characterization based on envelope statistics ; the Results section presents results from the 112 lymph nodes studied to date; and finally, the Discussion section presents a detailed overview of the study to date and the next steps of the study.

METHODS

Surgery, lymph-node preparation, and ultrasound data acquisition

The surgery, lymph-node preparation and ultrasound data-acquisition protocols for this study were identical to the previously-described protocols (Mamou et al, 2010), and they are summarized below for completeness. Lymph nodes were dissected from patients with histologically-proven primary cancers at the Kuakini Medical Center (KMC) in Honolulu, HI. The dissected nodes were prepared for pathology according to the current standard of care for surgical treatment of colorectal and stomach cancers. After surgical excision, dissected nodes were brought to the pathologist for gross preparation. Then, individual, manually-defatted lymph nodes were placed in a water bath containing isotonic saline (0.9% sodium chloride solution) at room temperature and ultrasonically scanned while pinned through a thin margin of fat to a piece of sound-absorbing material.

Ultrasound data were acquired with a focused, single-element transducer (PI30-2-R0.50IN, Olympus NDT, Waltham, MA) that had an aperture of 6.1 mm and a focal length of 12.2 mm. The transducer had a center frequency of 25.6 MHz and a -6-dB bandwidth that extended from 16.4 to 33.6 MHz. The theoretically predicted axial and lateral resolutions of the HFU imaging system were 43 and 116 μm , respectively. The 6-dB depth of field was measured to be 1.6 mm extending from 11.4 mm to 13.0 mm. The transducer was excited by a Panametrics 5900 pulser/receiver unit (Olympus NDT, Waltham, MA), and the radio-frequency (RF) echo signals were digitized using an 8-bit Acqiris DB-105 A/D board (Acqiris, Monroe, NY) at a sampling frequency of 400 MS/s. The spacing between adjacent A-lines was 25- μm . A 3D scan of each lymph node was obtained by scanning adjacent planes uniformly spaced every 25 μm over the entire lymph node. The RF data were oversampled to limit noise effects and to increase the robustness of some of the processing steps (e.g., 3D segmentation and attenuation compensation).

Three-dimensional backscatter and envelope characterization methods

Two different approaches were used to characterize and quantify the microstructural tissue properties of lymph nodes. The first approach was based on backscatter spectral quantification and the second approach modeled the envelope statistics of the backscattered signal. These two approaches were used to test the hypothesis that QUS estimates obtained from backscatter spectral and envelope quantification are statistically different between cancerous (i.e., metastatic) and non-cancerous tissue in lymph nodes. Subsequent sections in this paper describe in great detail the envelope-statistics quantification, but they only briefly review the methods used for backscatter spectral quantification because they were previously published (Mamou et al, 2010).

Three-dimensional segmentation and cylindrical regions of interest

The 3D RF data sets were segmented using a semi-automatic algorithm to separate nodal tissue, from saline and remaining fibroadipose tissue. The segmentation algorithm has been presented and evaluated in great detail before and has not been modified significantly except for improvements in its computational efficiency (Coron et al, 2008; Mamou et al, 2010). Following segmentation, the complete 3D RF data set was separated into overlapping 3D cylindrical regions-of-interest (ROIs) having a diameter of 1 mm and a length (i.e., along the axis of the transducer) of 1 mm. The size of the ROI was chosen based on the resolution cell of our imaging system. The overlap between adjacent ROIs depended on the total number of voxels of the 3D RF data set; it was adjusted to permit smaller data sets to have a sufficient number of ROIs for statistical stability and to avoid overly-long computation times for larger data sets. (See Table 1 in (Mamou et al, 2010).)

Parameter estimation and QUS-image formation

Estimates of spectral intercept (I in dB), spectral slope (S in dB/MHz), effective scatterer sizes (D in μm) and acoustic concentration (i.e., CQ^2 expressed in dB mm^{-3}) were obtained using the previously published methods (Mamou et al, 2010). Briefly, these estimates were computed by fitting two different scattering models to normalized and attenuation-compensated ROI power spectra. Specifically, I and S were obtained by fitting a straight line to normalized ROI power spectra and D and CQ^2 were obtained assuming a spherical Gaussian scattering model (Mamou et al, 2010). Attenuation compensation was performed independently for each ROI, assuming straight-line propagation from the transducer surface to the ROI. This attenuation-compensation approach took into account propagation through fat and lymph-node tissue using two different attenuation values. The value for fat was estimated to be 0.97 dB/MHz/cm and the value for tissue was assumed to be 0.5 dB/MHz/cm; these values were assumed to be the same for every lymph node. Attenuation compensation previously was presented in great detail (Mamou et al, 2010).

In this study, four new QUS parameters were computed by fitting distribution models to the envelope statistics of each ROI. The first two parameters α and Ω were obtained using a maximum-likelihood estimator to fit a Nakagami probability density function (PDF) to that of the ROI envelope. The PDF of the Nakagami distribution is (Nakagami, 1960):

$$f_{\text{Nakagami}}(r) = \frac{2\alpha^\alpha r^{2\alpha-1}}{\Gamma(\alpha)\Omega^\alpha} \exp\left(-\frac{\alpha}{\Omega}r^2\right) U(r), \quad (1)$$

where Γ and U are the Gamma function and unit step function, respectively. The parameter Ω is termed the scaling parameter while α is usually called the Nakagami parameter. If R is a random variable with a Nakagami PDF, then

$$\Omega = E[R^2], \text{ and} \quad (2)$$

$$\alpha = \frac{(E[R^2])^2}{E[(R^2 - E[R^2])^2]}, \quad (3)$$

where E is the expected-value operator. The likelihood ratio was obtained by assuming that every envelope value within the ROI was independently and identically distributed. Then, the parameters α and Ω were found by maximizing the likelihood ratio using a descent algorithm.

The Nakagami parameter is a shape parameter for the PDF, and when it is equal to 1, the Nakagami distribution reduces to a Rayleigh distribution. Additionally, when α is between 0 and 1, the envelope distribution is said to be pre-Rayleigh (Nakagami, 1960). Finally, when $\alpha > 1$, the distribution is said to be post-Rayleigh (Shankar, 2000). When the ROI contains randomly-located scatterers with varying scattering cross sections, the envelope statistics are likely to be pre-Rayleigh and α is typically between 0.5 and 1 (Shankar, 1995). Similarly, when some spatial periodicity exists among scatterers within the resolution cell, then the envelope statistics are Rician or post-Rayleigh, and α becomes larger than unity (Shankar, 2000). Typically, α is used as a means to quantify the effective number of scatterers in the resolution cell. This interpretation can be obtained by noting that the random variable, $Z =$

R^2 , follows a Gamma distribution and interpreting the physical relationships between α and the effective number obtained from the Gamma distribution (Shankar et al, 2001).

Two additional QUS parameters, k and μ , were obtained using the HK distribution to model the envelope statistics within the ROI. The HK distribution was first introduced in 1980 (Jakeman, 1980). This distribution incorporates a capability to model situations with low or high scatterer densities, but also includes a capability to model situations where a coherent signal component exists because of periodically located scatterers (Dutt and Greenleaf, 1994).

The PDF of the HK distribution is given by the following integral expression:

$$f_{HK}(r) = r \int_0^{+\infty} x J_0(sx) J_0(rx) \left(1 + \frac{x^2 \sigma^2}{2\mu}\right)^{-\mu} dx, \quad (4)$$

where J_0 is the zeroth-order Bessel function of the first kind, s^2 is the coherent signal energy, σ^2 is the diffuse signal energy, and μ is a measure of the effective number of scatterers per resolution cell. A derived parameter, $k = s/\sigma$, the ratio of the coherent to the diffuse signal, can be used to describe the degree of structure or periodicity in scatterer locations. (No closed-form expression exists for f_{HK} , but a truncated converging series is used in practice (Hao et al, 2002).) We estimated k and μ for the HK distribution. Because of the complexity of Eq. (4), no straightforward method exists to obtain these estimates. Methods using the first three even moments have been described, but were computationally expensive and could lead to complex estimates (Dutt and Greenleaf, 1994). Instead, we used an algorithm that relied on moments of small orders (Hruska and Oelze, 2009). For completeness, the algorithm is summarized below.

The new algorithm extended previous work (Martin-Fernandez et al, 2007) and estimated envelope-statistics parameters by calculating the signal-to-noise ratio (SNR), skewness, and kurtosis of fractional-order moments of the envelope samples in each ROI. The use of fractional-order moments was motivated by previous studies (Dutt and Greenleaf, 1995; Ossant et al, 1998) that found that parameter estimates based on fractional-order moments were more robust than parameter estimates based on higher-order moments for the simpler, but related, K distribution. The optimal pair of fractional-order moments (i.e., 0.72 and 0.88) to use in the estimation routine was determined by construction of level curves for SNR, skewness, and kurtosis. The SNR, skewness (Sk_ν), and kurtosis (Ku_ν) of samples of the echo envelope of moment ν can be expressed as (Prager et al, 2002):

$$SNR_\nu = \frac{E[R^\nu]}{\left(E[R^{2\nu}] - E[R^\nu]^2\right)^{\frac{1}{2}}}, \quad (5)$$

$$Sk_\nu = \frac{E[R^{3\nu}] - 3E[R^\nu]E[R^{2\nu}] + 2E[R^\nu]^3}{\left(E[R^{2\nu}] - E[R^\nu]^2\right)^{\frac{3}{2}}}, \quad (6)$$

$$Ku_\nu = \frac{E[R^{4\nu}] - 4E[R^\nu]E[R^{3\nu}] - 6E[R^{2\nu}]E[R^\nu]^2 - 3E[R^\nu]^4}{(E[R^{2\nu}] - E[R^\nu]^2)^2}. \quad (7)$$

The optimal pair of fractional-order moments was found by calculating the maximal intersection angles between the six level curves generated at each pair of k and μ values over a range of values expected to be encountered in ultrasonic imaging (Hruska and Oelze, 2009). For a given ROI size, using the optimal moment orders results in the smallest variance of envelope-parameter estimates over the range of possible parameter space expected for ultrasonic imaging. Assuming homogeneous scattering statistics in the ROI, larger ROIs result in smaller bias and variance in parameter estimates because the parameter estimates depend on acquiring a good statistical representation of the signal envelope. The sizes of the ROIs chosen for parameter estimation in this study were sufficiently large to assure a good statistical representation of the underlying signal (Hruska, 2009).

Using this approach, estimates of the k and μ parameters for each ROI were obtained in three steps. First, the envelope of the signal was detected and the values of the envelope corresponding to the ROI location were stored in a vector. Second, the SNR, skewness, and kurtosis were calculated using Eqs. (5)-(7) for the vector of envelope values corresponding to the ROI using the chosen moment orders. Third, level curves previously generated and stored for the SNR, skewness, and kurtosis corresponding to different values of the k and μ parameters for the two fractional-order moments (i.e., 0.72 and 0.88) were used to find the intersection of the six level curves generated from the envelope values from the ROI in the k - μ plane.

The parameters μ and α were corrected to account for variations in the size of the resolution cell due to attenuation and diffraction effects. The correction algorithm multiplied the estimates by the term, κ , which varied for each ROI:

$$\kappa = \frac{B_{6\text{ dB}}^{ROI} [f_c^{ROI}]^2}{B_{6\text{ dB}} f_c^2}, \quad (8)$$

where f_c is the natural center frequency of the transducer (i.e., 25.6 MHz in the present case), $B_{6\text{ dB}}$ is the -6-dB bandwidth of the transducer (i.e., $33.6 - 16.4 = 17.2$ MHz), and f_c^{ROI} and $B_{6\text{ dB}}^{ROI}$ are the same quantities, but estimated within the ROI by taking into account diffraction effects (using the calibration spectrum acquired at the depth corresponding to the ROI center) and attenuation effects (based on the sound path from the transducer to the ROI). Details about the calibration spectrum and attenuation estimation were previously presented (Mamou et al, 2010). The rationale behind Eq. (8) is that the resolution cell of a

single-element system is proportional to $\frac{1}{B_{6\text{ dB}} f_c^2}$ (Kino, 1987). Therefore, multiplying estimates of μ and α by κ permits comparison (and averaging) of these QUS estimates among different ROIs and different lymph nodes.

The parameter, Ω , is the only envelope-statistics parameter sensitive to the absolute range of the envelope values within the ROI. For example, multiplying the envelope values by a constant, δ , changes the value of Ω by a factor of δ^2 , but does not change the values of α , k , and μ . Therefore, Ω is the envelope parameter that is most sensitive to attenuation and diffraction effects. To mitigate the effects of attenuation and diffraction on Ω , envelope

values for each ROI were multiplied by an ROI-dependent parameter, χ , which corrected for estimated attenuation and diffraction effects at 25.6 MHz, i.e., at the center frequency of the transducer:

$$\chi = S_{oil}(f, z_{ROI})A(f), \text{ with } f = 25.6 \text{ MHz}, \quad (9)$$

where z_{ROI} is the depth at the center of the ROI, S_{oil} is the calibration spectrum acquired at a depth equal to z_{ROI} and $A(f)$ is the attenuation-compensation function obtained for this ROI. The terms $A(f)$ and S_{oil} are defined in Eqs. (1) and (5) of (Mamou et al, 2010), respectively. Finally, because of their wide dynamic-range estimates, μ , α , and Ω were compressed using a base-10 logarithm function.

These eight QUS parameters were estimated for all adjacent ROIs within the entire segmented lymph-node tissue. 3D QUS images were formed by color-coding and overlaying the parameter values on the conventional B-mode volume. However, ROIs that were not fully contained in depths between $z = 10.8$ mm and $z = 13.5$ mm were not processed because they were judged to be too far away from the nominal focal depth of the transducer.

Materials used

The results described in the next section pertain to 112 lymph nodes excised from 77 different patients diagnosed with colorectal or gastric cancers. These lymph nodes either were entirely negative for metastases ($N = 92$), or were nearly completely filled with metastases ($N = 20$). The great majority (i.e., 98) of nodes were excised from colorectal-cancer patients, but 14 nodes acquired from gastric-cancer patients were also included in the study because of their availability. Although these lymph nodes were associated with cancers from different organs, they were grouped together for these studies because they present the same histopathologic features in healthy and diseased states (Mills, 2006). Combining nodes of gastric with colorectal cancers is reasonable histologically because the basic architecture of non-neoplastic lymph nodes is similar among different organ systems in healthy and diseased states (van der Valk and Meijer, 1987). Gastric and colorectal carcinomas are part of a diverse group of glandular epithelial neoplasms of the gastrointestinal tract that are composed of complex neoplastic glands in well- to moderately-differentiated lesions. Although subtle histologic differences may exist among them, these tumors generally present with the basic architecture of differentiated adenocarcinomas, i.e., neoplastic gland formation. From this standpoint, colorectal and gastric carcinomas and their metastases are similar histologically. Metastatic lesions to lymph nodes tend to retain the histologic appearance of the primary cancer, which is uniform among primary adenocarcinomas of the gastrointestinal tract, i.e., in gastric as well as colorectal cancers. Combining nodes in this manner is further justified by the results themselves, as presented in the next section. The nodes were diagnosed by a pathologist by looking at hematoxylin and eosin (H&E) stained sections.

The Institutional Review Boards (IRBs) of the University of Hawaii and the KMC approved the participation of human subjects in the study. All participants were recruited at KMC and gave written informed consent as required by both IRBs.

RESULTS

Illustrative parametric cross-section images and envelope PDFs

To illustrate the results of the 3D QUS processing, Fig. 1 displays the three B-mode cross sections of an entirely non-metastatic lymph node; each B-mode image is augmented by the color-coded estimates of $\log(\mu)$. A color bar and histogram of the entire node distribution of

$\log(\mu)$ are shown in Fig. 1d. The $\log(\mu)$ estimates show a fairly large distribution with a mean of -0.14 and a standard deviation of 0.22 . For comparison, Fig. 2 displays the $\log(\mu)$ cross sections of an entirely metastatic lymph node from a different patient. The color scales of Figs. 1 and 2 are the same for easier comparison. For this lymph node, the $\log(\mu)$ values were lower with a mean of -0.34 and a standard deviation of 0.22 . (The difference in the QUS voxel sizes between Figs. 1 and 2 is due to the change in overlap between adjacent ROIs depending on the total number of ultrasound voxels in the data set. (See Table 1 in (Mamou et al, 2010).))

The large variations in the estimates of $\log(\mu)$ shown in Figs. 1 and 2 illustrate how differentiating a metastatic node from a non-metastatic node potentially would be possible, but difficult using μ alone. The metastatic node globally has lower $\log(\mu)$ values and its QUS images are blue whereas the QUS images of the non-metastatic node contain some yellow and red in addition to some blue.

Typical cross-section images of other QUS parameters have been published previously and, in particular, scatterer-size images demonstrated significant potential for diagnosis and cancer localization (Mamou et al, 2010, 2009b,c).

Figures 3a and 3b display the estimated PDFs from two ROIs located near the center of each of the lymph nodes displayed in Figs. 1 and 2. The Nakagami and HK fit obtained using our estimators are also shown. In the case of the HK model, our estimator only returns two (μ and k) of the three independent parameters of the HK model, Eq. (4). The third parameter, σ , was obtained from the second-order moment of the HK distribution (Hruska and Oelze, 2009):

$$\sigma = \sqrt{\frac{E[R^2]}{k^2 + 2}}. \quad (10)$$

Examination of Figs. 3a and 3b indicates that the ROI PDFs are fitted better using the HK model because smaller root-mean-squared-errors (RMSEs) were obtained. Additionally, these figures demonstrate that both estimated PDFs are not satisfactorily fit using the Nakagami model. Another interesting feature is that the values of the RMSEs from both models obtained in the case of the metastatic node (Fig. 3b) are more than twice those obtained in the case of the non-metastatic node (Fig. 3a).

Lymph-node classification based on QUS estimates

For each lymph node, we averaged the eight QUS estimates over all of the ROIs that returned QUS estimates. The estimation algorithm was set to reject all QUS estimates from ROIs for which the scatterer-size estimate was smaller than $5 \mu\text{m}$. The algorithm also included a noise threshold to exclude ROIs for which the noise was judged to be too significant (Mamou et al, 2010). In the current study, over 98% of all ROIs of all nodes returned QUS estimates and only six lymph nodes had ROIs in which the algorithm did not return estimates. Using the averaged estimates, we evaluated whether correctly classifying lymph nodes was possible based on these eight QUS estimates. Table 1 displays the average and standard deviations of the QUS estimates for the metastatic and non-metastatic nodes.

The statistics of the four QUS estimates based on backscatter quantification are in strong agreement with our previously published results derived from a significantly lower number of lymph nodes (Mamou et al, 2010). The trend observed in Table 1 indicates that metastatic nodes have significantly larger effective scatterer-size estimates (i.e., D) and higher intercept

estimates (i.e., D), and significantly lower slope (i.e., S) and acoustic-concentration estimates (i.e., CQ^2). (Note that the ANOVA test showed statistical differences ($p < 0.05$) in metastatic and non-metastatic values for these four QUS parameters, which confirms results previously obtained with significantly fewer lymph nodes (Mamou et al, 2010).

The other four QUS estimates were obtained from the envelope statistics and the two distribution models (Table 1). No statistically significant differences were observed between the cancer-free and cancer-filled nodes for $\log(\Omega)$ and k , but estimates of $\log(\alpha)$ and $\log(\mu)$ were significantly lower in the metastatic lymph nodes. This is consistent with the physical interpretation of μ and α being related to scatterer number density. Metastatic nodes, which have larger effective scatterer-size estimates than non-metastatic nodes, are likely to have a concomitantly lower number density. Note that although statistically significant differences were observed for μ and α , the standard deviations of the estimates were fairly large and significant overlap existed between the estimates obtained between the two types of nodes. This also was illustrated in Figs. 1d and 2d for the μ parameter.

To visually illustrate the potential of the eight QUS estimates for classification, Fig. 4 displays the scatter plots of the QUS estimates obtained for the two different scattering models and the two different envelope-statistics models. Figure 4a shows good separation between the metastatic and non-metastatic nodes for size and concentration estimates. Some overlap exists in the range of sizes between 31 and 35 μm , but overall, the spherical Gaussian form-factor estimates show strong potential for detection of metastases. Similarly, Fig. 4b shows satisfactory separation, but more overlap is visible for S values between 0.05 and 0.22 dB/MHz. The other two panels show the results obtained by modeling envelope statistics with the Nakagami distribution (Fig. 4c) and the HK distribution (Fig. 4d). Overall, very poor separation is apparent; only a suggestion of smaller α and μ values is observed for metastatic nodes. This observation is consistent with the values reported in Table 1. Nevertheless, Fig. 4d reveals an interesting feature of the k estimates: every lymph node with an average value below 0.40 is non-metastatic and therefore, although the means of the k estimates are not statistically different (Table 1), the spread of the k estimates is larger for the non-metastatic nodes. This observation also indicates that nodes for which the incoherent signal energy is at least 2.5 times greater than the coherent signal energy are non-metastatic. In Fig. 4, the data points outlined in black denote the gastric-cancer nodes. These scatter plots suggest that all QUS estimates obtained from gastric-cancer nodes are very similar to those obtained from colorectal-cancer nodes for metastatic and non-metastatic node types. (For both node types, the ANOVA test failed to find a statistical difference between gastric and colorectal nodes for any of the eight QUS estimates.)

To further quantify these observations, the software package SPSS (SPSS Inc., Chicago, IL) was used to generate ROC curves for each individual QUS estimate and for several combinations of the eight QUS estimates using linear-discriminant analysis (Table 2). SPSS also was employed to evaluate classification performance using a leave-one-out procedure and the resulting specificity, sensitivity and percentage of correctly-classified nodes were computed (Table 2). Looking first at the numbers obtained with the four QUS estimates quantifying backscatter power spectra, the results indicate that using D alone, nearly perfect classification performance can be achieved with an area under the ROC curve (AUC) of 0.986 ± 0.009 . Specificity and sensitivity also were excellent with both values above 91%. The moderate overlap among the acoustic-concentration values (Fig. 4a) produced an AUC value of 0.829 ± 0.056 , a specificity of 80%, and a sensitivity of 70%; therefore, acoustic-concentration estimates alone would classify lymph nodes only moderately well. Finally, combining D and CQ^2 only marginally improves classification performance over D alone (AUC value of 0.988). I alone performs moderately well and as well as CQ^2 alone, and S performs well with a performance only slightly inferior to D alone. Finally, combining I and

S together produces an AUC value of 0.970 ± 0.015 , with sensitivity and specificity values of 90%.

Results for the other four QUS estimates based on envelope statistics indicate that diagnostic performance using any of these estimates alone would be unsatisfactory. AUC values obtained from Ω or k were smaller than 0.6. The Nakagami parameter, α , performed significantly better, but it still produced a mediocre AUC value of 0.768. Finally, the best performance was obtained using μ leading to an AUC value of 0.815, with sensitivity and specificity values above 70%. Interestingly, combining the Nakagami model parameters, α and Ω , led to an AUC value of 0.848, meaning that the Nakagami envelope model would classify lymph nodes moderately well. However, combining the two HK model parameters, k and μ , did not improve classification performance over μ alone. Nevertheless, the HK and Nakagami model classification performance only remains moderately satisfactory. These results indicate that the HK model produced the best QUS estimate (i.e., μ) for classification based on envelope quantification, but they also indicate that the Nakagami model slightly outperformed the HK model when the two independent QUS estimates from each model were combined.

Interestingly, the best classification results were obtained by combining D and k , which led to an AUC value of 0.996 ± 0.003 and sensitivity and specificity values of 95%. (No other combination of two or more QUS estimates led to a better performance.) Figure 5 shows the scatter plot of these two parameters and indicates that the separation between the cancer-containing and cancer-free nodes is better than on any of the other scatter plots shown in Fig. 4. Although the mean and standard deviation of k between each node type were essentially the same (Table 1), this parameter was able to improve classification performance over D alone. To investigate this fact, we looked at the distribution of k values among the nodes that had D estimates between 28.4 and 37.0 μm . This range of sizes was obtained by considering the mean of the two average values of D for each node class (i.e., 32.7 μm) and adding or removing the ensemble standard deviation of D (i.e., 4.3 μm). This procedure led to the selection of 60 nodes (49 non-metastatic nodes and 11 metastatic nodes) that had overlapping values of D for non-metastatic and metastatic nodes. The average k estimates within this selection were found to be 0.61 ± 0.11 and 0.53 ± 0.12 for metastatic and non-metastatic nodes, respectively. Additionally, the ANOVA test returned a p -value of 0.067 for these k estimates. These numbers indicate that in the region where a classifier based on D alone would be most likely to make classification errors, k estimates tend to be different for non-metastatic and metastatic nodes, and can positively influence classification performance; this is consistent with Table 2 and Fig. 5.

Additionally, Fig. 5 illustrates how a 100%-specificity or a 100%-sensitivity classifier could be designed using a linear combination of k and D . The green solid line passes through the two non-metastatic lymph nodes that are the closest to the mean of all the metastatic nodes; therefore, if this line is established as a classifier threshold and all nodes above the line are declared to be metastatic and all nodes below the line to be non-metastatic, then 100% specificity will be achieved with a sensitivity of 90%. Similarly, the red solid line would lead to a classifier with 100% sensitivity (all metastatic nodes are classified correctly) at a specificity of 97.5%. Clinically, the 100% sensitivity approach is more relevant; it guarantees that no cancer will be missed and potentially could significantly reduce the number of nodes requiring histological evaluation by reliably identifying cancer-free nodes, and more important, could identify suspicious regions for detailed histological evaluation that contain small metastases that would be overlooked using standard histology procedures. Here, instead of 112 nodes, only 22 would be sent to histology and no cancer would be overlooked. These methods would serve as an adjunct to histopathology that would improve the efficiency of histological procedures for node evaluations.

In summary, Tables 1 and 2 and Figures 4 and 5 present very satisfactory results. Our QUS methods are able to classify the nodes that either are completely metastatic or are completely free of metastatic tissue nearly perfectly using only one (D) or two QUS estimates (D and k). Finally, based on the current results, the spherical Gaussian scattering model slightly outperforms the straight-line model. Additionally, the results indicate that of the four QUS estimates from the two proposed envelope models, the μ parameter obtained from the more-advanced HK model provides the best classification performance.

DISCUSSION

The studies presented herein initially were motivated by earlier studies performed at lower frequencies (i.e., 10 MHz) that suggested spectral intercept estimates produced a very high AUC value for lymph-node classification (Feleppa et al, 1997). More-recent studies performed at higher frequencies on 46 lymph nodes resulted in perfect classification using D or S alone (Mamou et al, 2010). Subsequently, we significantly extended these studies by investigating 112 lymph nodes, and also quantifying envelope statistics using a commonly-used classic model (i.e., Nakagami) and a more-involved model (HK) employing an efficient and robust algorithm (Hruska and Oelze, 2009).

Estimating the four QUS envelope parameters using a maximum-likelihood estimator for α and Ω and the fractional-order moment algorithm for μ and k increased computation time by only 15% when compared to estimating only the four other QUS estimates; however, computation times remained far from real-time. To obtain the eight QUS estimates for an entire lymph node required an average time of 20 minutes. In their present form, all the algorithms were implemented in MATLAB (The Mathworks Inc., Natick, MA) because of its convenience for research-oriented signal and image processing. Nevertheless, this time frame is amenable to intraoperative characterization. (Conventional histology usually takes at least one day to provide diagnostic results.) Eventually, the final algorithms will be converted and compiled as efficient executables using C++. Additionally, once we have isolated the best QUS estimates for classification, only those would need to be computed. For example, based on the results to date and presented in Table 2, only k and D would need to be estimated. A decrease in computation time of about 30% was observed when only estimates of k and D were computed for an entire lymph node using MATLAB.

The 3D QUS methods presented in this study permitted virtually perfect classification of a relevant number of lymph nodes that either were nearly completely metastatic or were entirely non-metastatic. Therefore, in the future, we will apply and evaluate these methods in studies of lymph nodes with smaller micrometastatic foci that do not fill the node. The hypothesis we will test in partially-metastatic lymph nodes is that 3D QUS estimates can reliably detect small cancer-containing regions including clinically-significant micrometastasis. Because we also have the 3D histology data with histologically-defined cancer regions, we easily will be able to evaluate the performance of the QUS methods. In particular, an important question would be to determine the smallest size of metastatic foci that we can detect. To detect clinically-relevant micrometastases (i.e., diameter between 0.2 mm and 2 mm), we may need to decrease the size of the ROIs to improve the QUS-image spatial resolution. Based on empirical published criteria, using cylindrical ROIs with a diameter of 0.6 mm and a length of 0.4 mm with our imaging system should not increase bias or variance of QUS estimates quantifying backscatter significantly (Oelze and O'Brien, 2004a), but such ROIs would significantly improve 3D QUS image resolution. Further resolution improvements also may be possible using methods that correct for ROIs with sub-optimal lengths (Oelze and O'Brien, 2004b). Additionally, another option would be to use an ultrasound transducer with a higher center frequency, which would allow smaller ROIs;

however, the trade-off would be the decreased penetration depth of the higher-frequency ultrasound and therefore a reduced ability to obtain QUS estimates deep into lymph nodes.

In this study, the same ROIs used for the spectral estimates were used to produce the envelope statistics. Envelope statistics are notorious for large variances if the sample size (i.e., the size of the ROI) is too small. In the future, the variances of the envelope statistics could be reduced with larger ROIs. Regions of suspicion within a node could be determined based on estimates of effective scatterer size. Within the suspicious regions, larger ROIs could be selected to produce envelope-statistics estimates with smaller variances. Envelope statistics would produce images with poorer spatial resolution, but with improved classification resulting from a reduction in the variance of the estimates.

Finally, we have initiated analyses of RF data from axillary lymph nodes, including sentinel nodes of breast-cancer patients based on what we have learned from the more-available and architecturally simpler abdominal nodes of colorectal- and gastric-cancer patients. Axillary nodes present complications associated with intra-nodal inclusions, which appear to be small fatty deposits. Therefore, our approach must be modified to exclude these fatty regions from QUS processing. To achieve this goal, efforts are being directed toward improving the 3D segmentation methods to detect these regions even though they are surrounded by nodal tissue.

Acknowledgments

NIH Grant CA100183 supported these studies in part. The authors thank Helena Herman and Justin Rhoda for their help with the 3D segmentation of the lymph nodes.

References

- Aristizábal O, Christopher DA, Foster FS, Turnbull DH. 40-MHz echocardiography scanner for cardiovascular assessment of mouse embryos. *Ultrasound Med. Biol.* 1998; 24(9):1407–1417. [PubMed: 10385963]
- Baddour RE, Sherar MD, Hunt JW, Czarnota GJ, Kolios MC. High-frequency ultrasound scattering from microspheres and single cells. *J Acoust Soc Am.* 2005; 117:934–943. [PubMed: 15759712]
- Coron, A.; Mamou, J.; Hata, M.; Machi, J.; Yanagihara, E.; Laugier, P.; Feleppa, EJ. Three-dimensional segmentation of high-frequency ultrasound echo signals from dissected lymph nodes. *Proceedings of the 2008 IEEE Ultrasonics Symposium*; 2008. p. 1370-1373.
- de Korte CL, van der Steen AFW, Céspedes EI, Pasterkamp G, Carlier SG, Mastik F, Schoneveld AH, Serruys PW, Bom N. Characterization of plaque components and vulnerability with intravascular ultrasound elastography. *Phys. Med. Biol.* 2000; 45(6):1465–1475. [PubMed: 10870704]
- Destrempe F, Cloutier G. A critical review and uniformized representation of statistical distributions modeling the ultrasound echo envelope. *Ultrasound Med Biol.* 2010; 36(7):1037–51. [PubMed: 20620691]
- Dutt V, Greenleaf JF. Ultrasound echo envelope analysis using a homodyned K distribution signal model. *Ultrason Imaging.* 1994; 16:265–287. [PubMed: 7785128]
- Dutt V, Greenleaf JF. Speckle analysis using signal to noise ratios based on fractional order moments. *Ultrason Imaging.* 1995; 17(4):251–268. [PubMed: 8677561]
- Eltoft T. The rician inverse gaussian distribution: a new model for non-rayleigh signal amplitude statistics. *IEEE Transactions on Image Processing.* 2005; 14(11):1722–1735. [PubMed: 16279173]
- Feleppa EJ, Lizzi FL, Coleman DJ, Yaremko MM. Diagnostics spectrum analysis in ophthalmology: a physical perspective. *Ultrasound Med. Biol.* 1986; 12:623–631. [PubMed: 3532476]
- Feleppa, EJ.; Machi, J.; Noritomi, T.; Tateishi, T.; Oishi, R.; Yanagihara, E.; Jucha, J. Differentiation of metastatic from benign lymph nodes by spectrum analysis in vitro. *Proceedings of the 1997 IEEE Ultrasonics Symposium*; 1997. p. 1137-1140.

- Hao X, Bruce CJ, Pislaru C, Greenleaf JF. Characterization of reperfused infarcted myocardium from high-frequency intracardiac ultrasound imaging using homodyned K distribution. *IEEE Trans Ultrason Ferroelectr Freq Control*. 2002; 49(11):1530–1542. [PubMed: 12484476]
- Hruska, DP. M.S. Thesis. University of Illinois at Urbana-Champaign; 2009. Improved techniques for statistical analysis of the envelope of backscattered ultrasound using the homodyned K distribution.
- Hruska DP, Oelze ML. Improved parameter estimates based on the homodyned K distribution. *IEEE Transactions on Ultrasonics, Ferroelectrics, and Frequency Control*. Nov.; 2009 56(11):2471–2481.
- Hruska, DP.; Sanchez, J.; Oelze, ML. Improved diagnostics through quantitative ultrasound imaging. *Proc. Annual International Conference of the IEEE Engineering in Medicine and Biology Society EMBC 2009*; 2009. p. 1956-1959.
- Huang YP, Zheng YP, Leung SF, Choi AP. High frequency ultrasound assessment of skin fibrosis: clinical results. *Ultrasound Med. Biol*. 2007; 33:1191–1198. [PubMed: 17467155]
- Insana MF, Wagner RF, Brown DG, Hall TJ. Describing small-scale structure in random media using pulse-echo ultrasound. *J. Acoust. Soc. Am*. 1990; 87:179–192. [PubMed: 2299033]
- Jakeman E. On the statistics of K distributed noise. *J. Phys. A: Math. Gen*. 1980; 13:31–48.
- Kino, GS. *Acoustic waves*. Prentice Hall; Englewoods Cliffs, NJ: 1987.
- Kolios MC, Czarnota GJ, Lee M, Hunt JW, Sherar MD. Ultrasonic spectral parameter characterization of apoptosis. *Ultrasound Med Biol*. 2002; 28:589–597. [PubMed: 12079696]
- Lizzi FL, Greenebaum M, Feleppa EJ, Elbaum M, Coleman DJ. Theoretical framework for spectrum analysis in ultrasonic tissue characterization. *J. Acoust. Soc. Am*. April.1983 73:1366–1373. [PubMed: 6853848]
- Mamou J, Aristizabal O, Silverman RH, Ketterling JA, Turnbull DH. High-frequency chirp ultrasound imaging with an annular array for ophthalmologic and small-animal imaging. *Ultrasound Med Biol*. 2009a; 35(7):1198–208. [PubMed: 19394754]
- Mamou J, Coron A, Hata M, Machi J, Yanagihara E, Laugier P, Feleppa EJ. High-frequency quantitative ultrasound imaging of cancerous lymph nodes. *Japanese Journal of Applied Physics*. 2009b; 48:07GK08–1–8.
- Mamou, J.; Coron, A.; Hata, M.; Machi, J.; Yanagihara, E.; Laugier, P.; Feleppa, EJ. Three-dimensional high-frequency characterization of excised human lymph nodes. *Proceedings of the 2009 IEEE Ultrasonics Symposium*; 2009c. p. 45-48.
- Mamou J, Coron A, Hata M, Machi J, Yanagihara E, Laugier P, Feleppa EJ. Three-dimensional high-frequency characterization of cancerous lymph nodes. *Ultrasound Med Biol*. 2010; 36:361–375. [PubMed: 20133046]
- Mamou J, Oelze ML, O'Brien WD Jr, Zachary JF. Extended three-dimensional impedance map methods for identifying ultrasonic scattering sites. *J Acoust Soc Am*. 2008; 123:1195–1208. [PubMed: 18247919]
- Martin-Fernandez, M.; Cardenes, R.; Alberola-Lopez, C. Parameter estimation of the homodyned K distribution based on signal to noise ratio. *IEEE International Ultrasonics Symposium*; New York, NY, USA. October 2007; p. 158-161.
- Mills, SE. *Histology for Pathologists*. third edition. Lippincott Williams & Wilkins; Philadelphia, Pa: 2006.
- Nakagami, M. *Statistical methods on wave propagation*. Pergamon Press; New York, NY: 1960. Ch. The m-distribution-A general formula of intensity distribution in rapid fading; p. 3-36.
- Oelze ML, O'Brien WDJ. Defining optimal axial and lateral resolution for estimating scatterer properties from volumes using ultrasound backscatter. *J Acoust Soc Am*. 2004a; 115(6):3226–34. [PubMed: 15237847]
- Oelze ML, O'Brien WDJ. Improved scatterer property estimates from ultrasound backscatter for small gate lengths using a gate-edge correction factor. *J Acoust Soc Am*. 2004b; 116(5):3212–23. [PubMed: 15603167]
- Oelze ML, Zachary JF. Examination of cancer in mouse models using high-frequency quantitative ultrasound. *Ultrasound Med Biol*. 2006; 32:1639–1648. [PubMed: 17112950]

- Oelze ML, Zachary JF, O'Brien WD Jr. Characterization of tissue microstructure using ultrasonic backscatter: Theory and technique for optimization using a Gaussian form factor. *J. Acoust. Soc. Am.* 2002; 112:1202–1211. [PubMed: 12243165]
- Ossant F, Patat F, Lebertre M, Teriierooiterai ML, Pourcelot L. Effective density estimators based on the K distribution: interest of low and fractional order moments. *Ultrason Imaging.* Oct; 1998 20(4):243–259. [PubMed: 10197346]
- Prager RW, Gee AH, Treece GM, Berman LH. Analysis of speckle in ultrasound images using fractional order statistics and the homodyned K distribution. *Ultrasonics.* 2002; 40:133–137. [PubMed: 12159920]
- Raju BI, Srinivasan MA. Statistics of envelope of high-frequency ultrasonic backscatter from human skin in vivo. *IEEE Transactions on Ultrasonics, Ferroelectrics, and Frequency Control.* 2002; 49(7):871–882.
- Saijo Y, Tanaka A, Owada N, Akino Y, Nitta S. Tissue velocity imaging of coronary artery by rotating-type intravascular ultrasound. *Ultrasonics.* 2004; 42:753–757. [PubMed: 15047378]
- Shankar PM. A model for ultrasonic scattering from tissues based on the K distribution. *Phys Med Biol.* 1995; 40(10):1633–49. [PubMed: 8532745]
- Shankar PM. A general statistical model for ultrasonic backscattering from tissues. *IEEE Transactions on Ultrasonics, Ferroelectrics, and Frequency Control.* May; 2000 47(3):727–736.
- Shankar PM, Dumane VA, Reid JM, Genis V, Forsberg F, Piccoli CW, Goldberg BB. Use of the K-distribution for classification of breast masses. *Ultrasound Med Biol.* 2000; 26(9):1503–1510. [PubMed: 11179624]
- Shankar PM, Dumane VA, Reid JM, Genis V, Forsberg F, Piccoli CW, Goldberg BB. Classification of ultrasonic B-mode images of breast masses using Nakagami distribution. *IEEE Trans Ultrason Ferroelectr Freq Control.* 2001; 48(2):569–580. [PubMed: 11370371]
- Silverman RH, Ketterling JA, Mamou J, Coleman DJ. Improved high-resolution ultrasonic imaging of the eye. *Arch Ophthalmol.* 2008; 126:94–97. [PubMed: 18195224]
- Silverman RH, Rondeau MJ, Lizzi FL, Coleman DJ. Three-dimensional high-frequency ultrasonic parameter imaging of anterior segment pathology. *Ophthalmology.* 1995; 102(5):837–843. [PubMed: 7777285]
- Tsui PH, Chang CC. Imaging local scatterer concentrations by the nakagami statistical model. *Ultrasound Med Biol.* Apr; 2007 33(4):608–619. [PubMed: 17343979]
- Tsui PH, Yeh CK, Liao YY, Chang CC, Kuo WH, Chang KJ, Chen CN. Ultrasonic Nakagami imaging: a strategy to visualize the scatterer properties of benign and malignant breast tumors. *Ultrasound Med Biol.* 2010; 36(2):209–217. [PubMed: 20018436]
- Tunis AS, Czarnota GJ, Giles A, Sherar MD, Hunt JW, Kolios MC. Monitoring structural changes in cells with high-frequency ultrasound signal statistics. *Ultrasound Med Biol.* 2005; 31(8):1041–9. [PubMed: 16085095]
- Turnbull DH. Ultrasound backscatter microscopy of mouse embryos. *Methods Mol. Biol.* 2000; 135:235–243. [PubMed: 10791320]
- Turnbull DH, Foster FS. Ultrasound biomicroscopy in developmental biology. *Trends Biotechnol.* 2002; 20:S29–S33.
- van der Valk P, Meijer CJ. The histology of reactive lymph nodes. *Am J Surg Pathol.* 1987; 11(11): 866–82. [PubMed: 3499826]
- Vogt M, Ermert H. In vivo ultrasound biomicroscopy of skin: spectral system characteristics and inverse filtering optimization. *IEEE Trans. Ultrason. Ferroelectr. Freq. Control.* 2007; 54:1551–1559. [PubMed: 17703658]
- Wagner RF, Insana MF, Brown DG. Statistical properties of radio-frequency and envelope-detected signals with applications to medical ultrasound. *J Opt Soc Am A.* 1987; 4(5):910–922. [PubMed: 3298583]

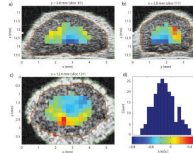


Figure 1.
a)-c): QUS cross-section images of $\log(\mu)$ of a non-metastatic lymph node. d) Histogram of $\log(\mu)$ estimates. White arrows in a) and b) indicate the focal depth of the transducer.

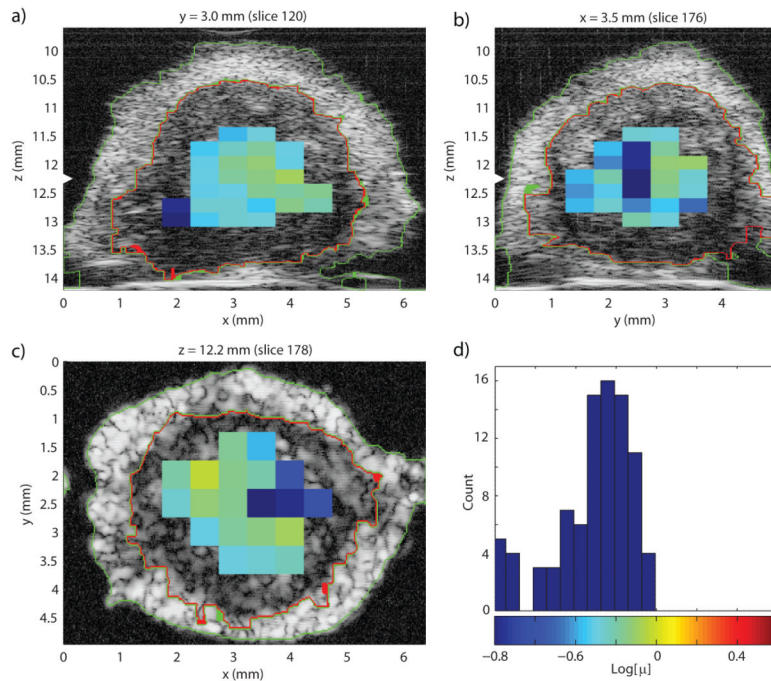


Figure 2.
a)-c): QUS cross-section images of $\log(\mu)$ of a completely metastatic lymph node. d) Histogram of $\log(\mu)$ estimates. White arrows in a) and b) indicate the focal depth of the transducer.

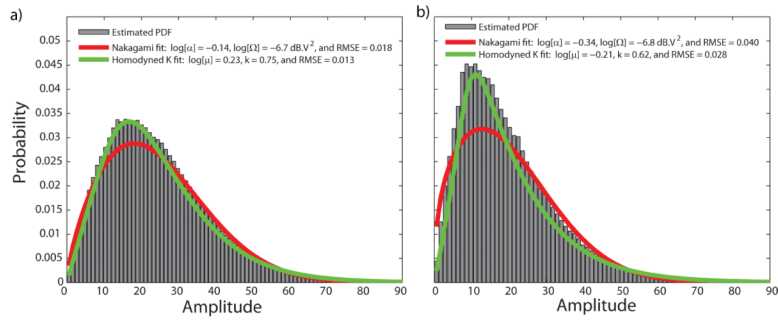


Figure 3.
 a)-b): Estimated PDF and overlaid fits using the Nakagami and HK PDFs of an ROI near the center of the lymph nodes shown in Figs. 1 and 2, respectively.

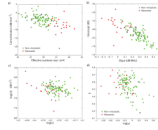


Figure 4. Scatter plots of estimates by model. a) Effective scatterer size and acoustic concentration (Gaussian form factor), b) intercept and slope (straight-line model), c) Nakagami envelope model and d) homodyned-K envelope model. Gastric cancer nodes are outlined in black.

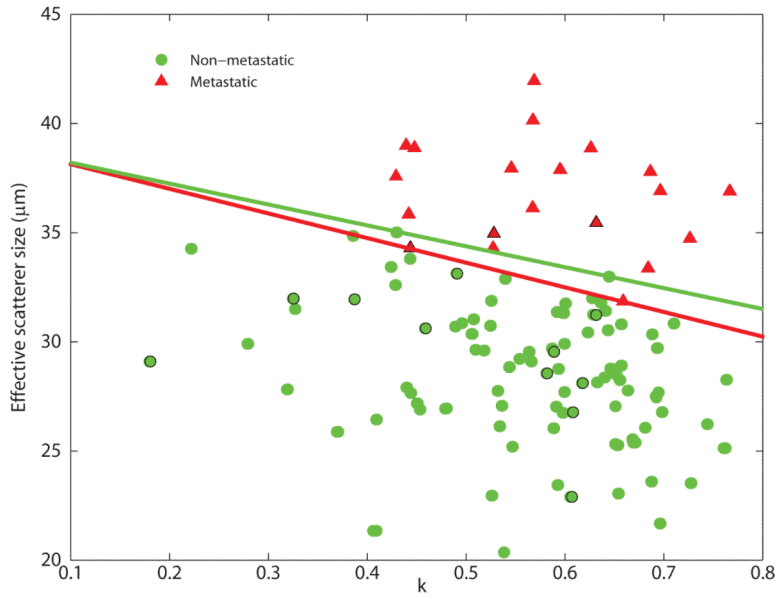


Figure 5. Scatter plot of best estimate combination for classification (k and D) and illustration of possible classification performance at 100% specificity (green solid line) or 100% sensitivity (red solid line). Gastric cancer nodes are outlined in black.

Table 1

Average QUS estimates (means \pm standard deviations) for non-metastatic and metastatic nodes. (The symbol “*” indicates statistical significance based on ANOVA results giving $p < 0.05$.)

QUS estimate	Non-metastatic nodes ($N = 92$)	Metastatic nodes ($N = 20$)
D (μm)	$28.6 \pm 3.1^*$	$36.7 \pm 2.5^*$
CQ^2 (dB mm^{-3})	$-3.73 \pm 2.48^*$	$-7.77 \pm 4.31^*$
I (dB)	$-63.1 \pm 3.8^*$	$-57.7 \pm 4.7^*$
S (dB/MHz)	$0.30 \pm 0.11^*$	$0.01 \pm 0.11^*$
$\log [\alpha]$	$-0.26 \pm 0.05^*$	$-0.32 \pm 0.06^*$
$\log [\Omega]$ (dB V^2)	-6.54 ± 0.22	-6.62 ± 0.39
$\log [\mu]$	$-0.09 \pm 0.19^*$	$-0.35 \pm 0.22^*$
k	0.56 ± 0.12	0.58 ± 0.10

Table 2

Classification performance analysis of the ability of QUS estimates to discriminate between metastatic and non-metastatic nodes. Areas under the ROC curve (AUC) include the standard errors in the area estimates. Sensitivity, specificity, and the percentage of correctly-classified nodes (P_c) were obtained using linear discriminant analysis with a leave-one-out procedure.

QUS Estimates	ROC AUC	95% Confidence	Sensitivity	Specificity	P_c
<i>D</i>	0.986 ± 0.009	0.969–1.000	95.0%	91.3%	92.0%
<i>CQ</i> ²	0.829 ± 0.056	0.719–0.939	70.0%	80.4%	78.6%
<i>D</i> and <i>CQ</i> ²	0.988 ± 0.009	0.971–1.000	95.0%	91.3%	92.0%
<i>I</i>	0.829 ± 0.058	0.716–0.942	75.0%	73.9%	74.1%
<i>S</i>	0.968 ± 0.016	0.936–0.999	90.0%	90.2%	90.2%
<i>I</i> and <i>S</i>	0.970 ± 0.015	0.940–1.000	90.0%	90.2%	90.2%
log [α]	0.768 ± 0.062	0.647–0.889	65.0%	70.7%	69.6%
log [Ω]	0.573 ± 0.077	0.422–0.724	60.0%	60.9%	60.7%
log [α] and log [Ω]	0.848 ± 0.053	0.743–0.952	70.0%	72.8%	72.3%
<i>k</i>	0.526 ± 0.072	0.384–0.667	55.0%	55.4%	55.4%
log [μ]	0.815 ± 0.058	0.702–0.929	70.0%	73.9%	73.2%
<i>k</i> and log [μ]	0.815 ± 0.058	0.702–0.929	70.0%	73.9%	73.2%
<i>D</i> and <i>k</i>	0.996 ± 0.003	0.989–1.000	95.0%	95.7%	95.5%